

Structural study of biotic and abiotic poorly-crystalline manganese oxides using atomic pair distribution function analysis

Mengqiang Zhu^{a,*}, Christopher L. Farrow^b, Jeffrey E. Post^c, Kenneth J.T. Livi^d, Simon J.L. Billinge^{b,e}, Matthew Ginder-Vogel^a, Donald L. Sparks^a

^a Department of Plant and Soil Sciences and Delaware Environmental Institute, University of Delaware, Newark, DE 19716, United States

^b Department of Applied Physics and Applied Mathematics, Columbia University, New York, NY 10027, United States

^c Smithsonian National Museum of Natural History, Washington, DC 20560, United States

^d HRAEM/IIC Departments of Biology and Earth and Planetary Sciences, Johns Hopkins University, Baltimore, MD 21218, United States

^e Condensed Matter Physics and Materials Science Department, Brookhaven National Laboratory, Upton, NY 11973, United States

Received 2 May 2011; accepted in revised form 5 December 2011

Abstract

Manganese (Mn) oxides are among the most reactive natural minerals and play an important role in elemental cycling in oceanic and terrestrial environments. A large portion of naturally-occurring Mn oxides tend to be poorly-crystalline and/or nanocrystalline, with not fully resolved crystal structures. In this study, the crystal structures of their synthetic analogs including acid birnessite (AcidBir), δ -MnO₂, polymeric MnO₂ (PolyMnO₂) and a bacteriogenic Mn oxide (BioMnO_x), have been revealed using atomic pair distribution function (PDF) analysis. Results unambiguously verify that these Mn oxides are layered materials. The best models that accurately allow simulation of pair distribution functions (PDFs) belong to the monoclinic *C12/m1* space group with a disk-like shape. The single MnO₆ layers in the average structures deviate significantly from hexagonal symmetry, in contrast to the results of previous studies based on X-ray diffraction analysis in reciprocal space. Manganese occupancies in MnO₆ layers are estimated to be 0.936, 0.847, 0.930 and 0.935, for AcidBir, BioMnO_x, δ -MnO₂ and PolyMnO₂, respectively; however, occupancies of interlayer cations and water molecules cannot be accurately determined using the models in this study. The coherent scattering domains (CSDs) of PolyMnO₂, δ -MnO₂ and BioMnO_x are at the nanometer scale, comprising one to three MnO₆ layers stacked with a high disorder in the crystallographic *c*-axis direction. Overall, the results of this study advance our understanding of the mineralogy of Mn oxide minerals in the environment.

© 2011 Elsevier Ltd. All rights reserved.

1. INTRODUCTION

Manganese (Mn) oxides are versatile materials, in terms of their use in industrial applications, and environmentally important role in biogeochemical elemental cycling. They can be used as cathodic materials in lithium batteries, molec-

ular sieves, and catalysts, etc. (Feng et al., 1995; Post, 1999). Mn oxide minerals affect carbon cycling (Shindo and Huang, 1982; Stone and Morgan, 1984), nutrient speciation (Shindo and Huang, 1984; Luther, 2002), and mobility, bioavailability and toxicity of metal(loid)s, e.g., arsenic (Zhu et al., 2009; Lafferty et al., 2010), via sorption and redox reactions in the environment. However, they are generally less abundant than other minerals, such as iron and aluminum (oxyhydr)oxides. Both layered and tunnel structures of Mn oxides have been identified in the environment with the former type more abundant, such as birnessite and birnessite-like minerals (Post, 1999). It is critical to know

* Corresponding author. Present address: Earth Sciences Division, Lawrence Berkeley National Laboratory, 307 McCone Hall, University of California-Berkeley, Berkeley, CA 94720-4767, United States. Tel.: +1 510 643 9120.

E-mail address: mzhu@lbl.gov (M. Zhu).

the detailed crystal structures of Mn oxides in order to better understand their behavior in geochemical processes. However, a major portion of naturally-occurring Mn oxide minerals, such as vernadite, are fine-grained and poorly-crystalline. This makes accurate crystal structure determination almost impossible using X-ray diffraction (XRD) Rietveld refinement since it is only suitable for well-crystallized materials (Post, 1999). Nevertheless, poorly crystalline Mn oxides are more actively involved in many important geochemical reactions than their well-crystallized counterparts due to their large surface area and enrichment of structural cation defects. In short, it is their poorly-crystalline nature that makes them both highly reactive and difficult to study. Therefore, it is important that methods be developed to unravel the complexities of these and similar materials.

Vernadite is the dominant Mn oxide phase precipitated in water bodies (e.g., sediments) and as coatings on other mineral surfaces (Chukhrov et al., 1979; Hochella et al., 2005; Bargar et al., 2009). Vernadite samples typically contain intimately mixed iron (oxyhydr)oxides as minor components, which further complicates their structural determination. Synthetic analogs, such as acid birnessite (AcidBir), δ -MnO₂ and polymeric MnO₂ (PolyMnO₂), have been used in investigating vernadite geochemical behavior in laboratory studies (McKenzie, 1980; Luther, 2002; Feng et al., 2007). These materials are poorly-crystalline and nanostructured with broad diffraction peaks at d-spacings of around 7, 3.5, 2.4 and 1.4 Å (Villalobos et al., 2003). They are generally thought to be layered materials consisting of turbostratically stacked MnO₆ octahedral layers (OL). MnO₆ octahedra in layers are connected by sharing edges only. Mn atoms in the layers are mainly Mn⁴⁺ but Mn³⁺ can be a minor component. The layers also contain varying amounts of cation defects (i.e., vacant sites). The presence of Mn³⁺ and vacant sites results in negative charge that is compensated by sorption of cations, such as H⁺ and metal cations, including Mn²⁺ and Mn³⁺, in the interlayer (IL) regions.

Vernadite formation is largely catalyzed by Mn-oxidizing microorganisms in oceanic and terrestrial environments (so called biogenic Mn oxides (BioMnO_x)) (Wehrli et al., 1995). BioMnO_x, produced by model marine and terrestrial bacteria, i.e., *Bacillus* sp. SG-1, *Pseudomonas putida* MnB1/GB-1 and *Leptothrix discophora* SP-6, have been characterized as layered Mn oxides by XRD and extended X-ray absorption fine structure (EXAFS) spectroscopy (Villalobos et al., 2003; Webb et al., 2005a; Saratovsky et al., 2009; Zhu et al., 2010a). These studies show that bacterial BioMnO_x samples have hexagonal layer symmetry, unless formed in the presence of cations, such as calcium, under relatively alkaline pH conditions (Webb et al., 2005b; Zhu et al., 2010a). However, the structure for BioMnO_x produced by fungi could be a tunnel type. A recent study, based on EXAFS analysis, proposed that *Acremonium* sp. KR21-2 produces a todorokite-like BioMnO_x (Saratovsky et al., 2009) in solid agar media. However, a layered structure of BioMnO_x, produced by the same type of bacteria, but in liquid media, was also reported (Grangeon et al., 2010). Todorokite and other tunnel Mn oxides are believed to be formed from layered Mn oxide precursors in the pres-

ence of template cations (Feng et al., 2010). These results suggest a direct formation pathway for todorokite from Mn²⁺ oxidation without layered Mn oxides as precursors.

EXAFS spectroscopy detects local atomic structure (within 6 Å) and cannot describe long-range order (Webb et al., 2005a). However, XRD Rietveld refinement reveals the detailed long-range ordered structure present in well-crystallized materials. These techniques, alone, are not capable of unambiguously characterizing the crystal structure of poorly-crystalline and nanoparticulate materials (Billinge and Levin, 2007). Consequently, XRD and EXAFS data of such complex materials can be variously interpreted or misinterpreted. Vernadite and δ -MnO₂ were proposed to be tunnel structures, i.e., todorokite and cryptomelane-like minerals, decades ago (Giovanoli, 1980; Manceau et al., 1992a,b). Even recently, Kim et al. (2003) proposed that BioMnO_x produced by *L. discophora* SP-6 is a todorokite-like structure based on EXAFS and Raman spectroscopy. However, this viewpoint has been disputed by more recent studies (Villalobos et al., 2003; Webb et al., 2005a; Saratovsky et al., 2006). Assuming layered structures, trial-and-error simulations of the poorly-defined XRD patterns of δ -MnO₂, acid birnessite and BioMnO_x provided geometrical dimensions using low angle data. Additionally, unit-cell parameters, atomic coordinates and occupancies of layer atoms and interlayer cations and H₂O molecules were determined using high angle data (Villalobos et al., 2006; Drits et al., 2007; Grangeon et al., 2010). These methods were also used for Ni-sorbed δ -MnO₂ samples to determine Ni positions (Grangeon et al., 2009). The results indicate that all of the above Mn oxides have hexagonal layer symmetry although discrepancies in positions of interlayer species remain. However, the crystallographic space group cannot be determined using the above methods.

Atomic pair distribution function (PDF) analysis is a total scattering technique, considering both Bragg and diffuse scattering. It probes not only the local structure but also intermediate and long-range order (Egami and Billinge, 2003). This makes PDF analysis an appropriate tool for investigating the structures of poorly-crystalline and nanoparticulate materials that yield diffraction patterns with large amounts of diffuse scattering between poorly-defined Bragg diffraction peaks (Egami and Billinge, 2003). A few structural determinations have been performed on poorly-crystalline Mn oxides using PDF analysis. Gateshki et al. (2004) reported that Mn oxides, synthesized by reduction of KMnO₄ with LiI in aqueous and anhydrous solutions, are layered structures belonging to the hexagonal R $\bar{3}$ M space group. A study by Petkov et al. (2009) suggested that BioMnO_x produced by *L. discophora* SP-6 bacteria and the fungus *Acremonium* sp. KR21-2 have birnessite (triclinic space group, *P1*) and todorokite-like (monoclinic space group, *P12/M1*) structures, respectively. This study supports the todorokite-like structure proposed by Saratovsky et al. (2009) using XAFS and XRD analyses. However, the triclinic space group of SP-6 BioMnO_x (deviating significantly from hexagonal symmetry) is contradictory to the hexagonal layer symmetry reported for BioMnO_x, that was produced under similar solution conditions (Villalobos et al., 2003; Zhu et al., 2010a).

In the present study, we applied X-ray PDF analysis to investigate the structures of the vernadite analogs, including BioMnO_x produced by *P. putida* GB-1, δ-MnO₂, PolyMnO₂ and AcidBir. The BioMnO_x used in this study was produced by a different strain of Mn-oxidizing bacteria than was reported in the previous PDF study (Petkov et al., 2009) to determine whether the structure of BioMnO_x depends on bacterial producers. The above materials are widely used model minerals in environmental science and biogeochemistry research. However, structural information is ambiguous, and in the case of PolyMnO₂, unknown. The PDF analysis in this study provides more rigid constraints on the Mn oxide crystal structures than previously available.

2. MATERIAL AND METHODS

2.1. Preparation of Mn oxides

Pyrolusite (1 × 1 Mn⁴⁺ tunnel structure) was purchased from Sigma–Aldrich. Todorokite was provided by the Smithsonian National Museum of Natural History. The sample was originally collected from Monte Negro Mine, Oriente Province, Cuba. Cryptomelane (2 × 2 Mn⁴⁺ tunnel structure), manganite (γ-MnOOH, 1 × 1 Mn³⁺ tunnel structure), triclinic birnessite (TrBir, Mn^{3/4+}, layered structure), hexagonal birnessite (HexBir, Mn^{2/3/4+}, layered structure), Acid birnessite (AcidBir), BioMnO_x, δ-MnO₂ and PolyMnO₂ were synthesized in the laboratory using standard procedures described below.

Cryptomelane was synthesized using the modified procedure of McKenzie (McKenzie, 1971; Feng et al., 2007). Eighty milliliters of 0.4375 M KMnO₄ solution was heated to 60 °C and poured into a 100 mL solution containing 0.5 M MnSO₄ and 2 M CH₃COOH at 60 °C. The mixture was heated and boiled while stirring for 20 min. A suitable amount of 2 M CH₃COOH was added to account for the volatilized CH₃COOH during the reaction. The suspension was cooled and centrifuged, and the collected precipitate was washed with DI water until the conductance of the supernatant was below 2 mS cm⁻¹. The solid was then aged in deionized (DI) water at 50 °C for 24 h, separated by centrifugation and then freeze-dried.

γ-MnOOH was synthesized according to Ramstedt et al. (2004). One hundred and fifty milliliters of 0.2 M ammonia was added to a mixture solution of 10.2 mL of 30% H₂O₂ and 500 mL of 0.06 M MnSO₄ (Ramstedt et al., 2004). The mixture was refluxed at 100 °C for 6 h under constant stirring. The brown solid was washed with hot DI water five times, separated by centrifugation, and then freeze-dried.

The synthesis of TrBir followed the method of Yang and Wang (2001, 2002) but without a thermal aging process. Two hundred and fifty milliliters of 0.4 M MnCl₂ solution and 250 mL of 8 M NaOH solution, prepared with anoxic DI water, were cooled to 0 °C in an ice-water bath before mixing. Upon mixing, pyrochroite (Mn(OH)₂) was immediately formed and the suspension was agitated by purging with N₂. The suspension appeared almost white in color. After 30 min, N₂ was quickly replaced with O₂, which was purged for 5 h. Pyrochroite was quickly oxidized to TrBir. Upon completion of these steps, a black suspension with a

blue tint was observed. The solid suspension was washed with DI water and then freeze-dried. MnO₆ layers in this product are not well stacked compared to the product synthesized using the thermal aging process (Yang and Wang, 2002).

HexBir was prepared by acidifying TrBir with nitric acid. To begin with, 1 g of freeze-dried TrBir was placed in 100 mL of a 0.1 M NaNO₃ solution in a plastic bottle. The suspension was dispersed ultrasonically and then acidified at pH 5 by adding 1 M HNO₃. The pH was maintained for 36 h using a pH STAT. The solid was collected by centrifugation, washed with DI water and then freeze-dried.

AcidBir was synthesized via reduction of KMnO₄ by HCl. 65.4 mL of concentrated HCl was added into 1 L of 0.4 M boiling KMnO₄ solution at 1 mL min⁻¹ using a peristaltic pump. A solid was formed and the suspension was stirred vigorously during the HCl addition. Due to the evaporation loss of HCl at the boiling temperature, KMnO₄ was not completely consumed, as indicated by the purple color of the suspension. The solid was collected by centrifugation, washed with DI water and then freeze-dried.

The synthesis of δ-MnO₂ employed a redox procedure between KMnO₄ and Mn(NO₃)₂ (Murray, 1975). Two hundred and fifty milliliters of 0.15 M Mn(NO₃)₂ was pumped at 20 mL min⁻¹, using a peristaltic pump, into a 250 mL solution containing 0.1 M KMnO₄ and 0.2 M NaOH. The reaction mixture was vigorously stirred during the Mn(NO₃)₂ solution addition. The solid suspension was collected by centrifugation, washed with DI water and air-dried.

The synthesis of PolyMnO₂ followed the procedure of Perez-Benito et al. (1989). Two hundred milliliters of 0.188 M Na₂S₂O₃ solution was pumped at 20 mL min⁻¹ into 200 mL of a 0.5 M KMnO₄ solution. The mixture was vigorously stirred during Na₂S₂O₃ addition. The precipitated suspension was collected by centrifugation, washed with DI water and air-dried.

BioMnO_x was produced by growing *P. putida* GB-1 at 30 °C in an 1800-mL Erlenmeyer flask that contained 500 mL of a *L. discophora* media. The flask was mixed at 200 rpm using a thermostatic orbital shaker. The *Leptothrix* media contained 0.5 g L⁻¹ yeast extract, 0.5 g L⁻¹ casamino acid, 1 g L⁻¹ glucose, 10 mM HEPES buffer (pH 7.5), 2 mM CaCl₂, 3.3 mM MgSO₄, 3.7 μM FeCl₃, 1 mL of trace element solution (10 mg L⁻¹ CuSO₄·5H₂O, 44 mg L⁻¹ ZnSO₄·7H₂O, 20 mg L⁻¹ CoCl₂·6H₂O, and 13 mg L⁻¹ Na₂MoO₄·2H₂O). Inocula were prepared by growing *P. putida* GB-1 bacterium in a media containing mineral salts, trace elements, and glucose (MSTG; 2 mM (NH₄)₂SO₄, 0.25 mM MgSO₄, 0.4 mM CaCl₂, 0.15 mM KH₂PO₄, 0.25 mM Na₂HPO₄, 10 mM HEPES, 0.01 mM FeCl₃, 0.01 mM EDTA, 1 mM glucose and 1 mL trace metal solution) for 12 h at 30 °C. After 24 h of growth, 2 mL of 0.1 M MnSO₄ were added (0.4 mM MnSO₄). The reaction was continued for another 24 h before collection of the solid. The final pH of the spent media was 7.48 and the dissolved Mn could not be detected by inductively coupled plasma atomic emission spectroscopy (ICP-AES). The solid was centrifuged multiple times at 1000g to remove loosely bound EPS, washed

with DI water and then air-dried. Bacterial material without addition of MnSO_4 was also prepared and air-dried. Diffraction data were also collected from this material and used as a background in the data analysis to deduce PDF data reflecting scattering only from Mn oxide in the BioMnO_x sample.

2.2. Chemical composition

The chemical composition of the above Mn oxides was determined by dissolving ~ 0.01 g dry powder in 50 mL solutions containing 0.1% $\text{NH}_3\text{OH}\cdot\text{HCl}$ and 1% HNO_3 . The solutions were then analyzed for metals by ICP-AES. The contents of Mg and Ca in the BioMnO_x sample might be overestimated since some Ca and Mg, originally associated with bacterial materials, could be desorbed in such an acidic solution (1% HNO_3). High resolution thermal gravimetric analysis (HR-TGA) was used to measure the water content of the samples. The temperature was gradually increased from 20 to 800 °C at 20 °C min^{-1} in a N_2 atmosphere. For TrBir, HexBir, AicdBir, $\delta\text{-MnO}_2$ and PolyMnO_2 the weight loss from 80 to 250 °C is attributed to the dehydration of structural water and the loss below 80 °C to physically sorbed water (Villalobos et al., 2003). The water content in the BioMnO_x was not measured due to the presence of volatile bacterial materials.

2.3. High resolution transmission electron microscopy (HRTEM)

A small amount of the solids was ultrasonically dispersed in DI water for 5 s. A Cu grid was dipped into the suspensions followed by air-drying. HRTEM analyses were performed on a Philips CM 300 FEG (field emission gun) operated at 297 kV. The spatial resolution of the CM 300 is 0.2 nm. Care was taken to avoid beam damage that can alter the structure of the Mn oxides.

2.4. X-ray diffraction experiments

X-ray diffraction experiments were conducted using X-rays of energy 58.290 keV ($\lambda = 0.2127 \text{ \AA}$) on beam line 11-ID-B at the Advanced Photon Source (APS), Argonne National Laboratory. Preliminary analyses were also conducted on beam line X7B at the National Synchrotron Light Source (NSLS). The high energy X-rays were used to extend the region of reciprocal space covered, which is necessary for high real-space resolution in the PDF. Finely ground powders of the samples were packed into polyimide (Kapton) tubing (Cole-Parmer 95820-09) with an inner diameter of ~ 1 mm. The measurements were performed using the rapid-acquisition PDF technique (Chupas et al., 2003), employing a Perkin Elmer amorphous silicon detector which was mounted orthogonally to the beam path. The image plate was exposed for 1 s and this was repeated 120 times for a total collection time of 120 s for each sample. Diffraction data on empty polyimide tubing, and tubing packed with dry powder of the bacterial material, were also collected for background removal in the PDF data reduction. Fit2D (Hammersley, 1998) was used to integrate and

convert 2-D data to 1-D intensity versus wave vector (Q). The sample-to-detector distance, beam center position and tilt angles of the detector, relative to the beam path, were calibrated using a CeO_2 standard provided by the beam line.

2.5. Atomic pair distribution function analysis

The PDF, $G(r)$, for a finite scattering body is defined as follows (Guinier, 1963; Farrow and Billinge, 2009):

$$G(r) = 4\pi r \gamma_0(r) [\rho_{\text{bulk}}(r) - \rho_0] \quad (1)$$

where $\rho_{\text{bulk}}(r)$ and ρ_0 are the local and average atomic number densities of an infinite body of the same internal structure as the finite body, respectively, $\gamma_0(r)$ accounts for the finite size and shape of the body and r is the radial distance. The PDF has peaks at characteristic distances separating pairs of atoms, and thus reflects the atomic structure. These peaks decrease in amplitude as r approaches the dimensions of the scattering body, thereby revealing its morphology.

The PDF is the Fourier transform of the experimentally observable total structure function (Egami and Billinge, 2003; Farrow and Billinge, 2009), $S(Q)$, i.e.,

$$G(r) = \frac{2}{\pi} \int_{Q_{\text{min}}}^{Q_{\text{max}}} F(Q) \sin(Qr) dQ \quad (2)$$

$$F(Q) = Q[S(Q) - 1] \quad (3)$$

where $F(Q)$ is the reduced structure function, Q is the magnitude of the wave vector where $Q = \frac{4\pi \sin\theta}{\lambda}$, 2θ is the angle between the incoming and outgoing radiation beams, and λ is the wavelength of the X-rays used. The structure function is related to the coherent part of the total diffraction intensity of the material as follows (Egami and Billinge, 2003):

$$S(Q) = 1 + \frac{[I^{\text{coh}}(Q) - (\sum c_i |f_i(Q)|^2)]}{|\sum C_i F_i(Q)|^2} \quad (4)$$

where $I^{\text{coh}}(Q)$ is the coherent scattering intensity per atom in electron units and c_i and f_i are the composition of the atomic species of type i and its X-ray scattering form factor, respectively.

In the Fourier transform step to get $G(r)$ from $S(Q)$ the data are truncated at a finite minimum, Q_{min} and maximum, Q_{max} values of the wave vector, Q . Different values of Q_{max} may be chosen. Here Q_{max} is optimized to avoid large termination effects while minimizing the statistical noise coming from the high- Q region where the signal-noise ratio becomes unfavorable. A $Q_{\text{max}} = 25.0 \text{ \AA}^{-1}$ was found to be optimal for poorly-crystalline samples. In order to compare PDF data between different samples, $Q_{\text{max}} = 25.0 \text{ \AA}^{-1}$ was also chosen for other well-crystallized samples. The total scattering structure function, $S(Q)$, and $G(r)$ were obtained using PDFgetX2 (Qiu et al., 2004), where standard corrections (Egami and Billinge, 2003) were applied as well as those unique to the area detector geometry (Chupas et al., 2003).

Structural information was extracted from the experimental PDFs using a full-profile real-space local-structure refinement method analogous to the Rietveld refinement.

The PDFs were modeled with a home written program SRREAL and refined with the aid of another home written program SRFIT for PDF modeling. Unlike PDFgui (Farrow et al., 2007), which only deals with a spherical shape for nanoparticles, SRFIT has characteristic functions for cylindrical and spheroidal scatters, and can work with various routines for better refinement convergence. In this investigation, we also made use of the ObjCryst++ library (Favre-Nicolin and Cerny, 2002) for increased computation speed with SRREAL. These factors have allowed us to repeatedly perform structure refinements with different optimization algorithms and many starting conditions to obtain structure models that are not accessible with PDFgui.

By following standard data reduction procedures, we were unable to obtain accurate intensity uncertainties, and thus the uncertainties of the experimental PDFs are unreliable. The standard procedure for estimating the uncertainties of refined parameters is to calculate the covariance matrix from the minimized χ^2 value of a refinement (Bevington et al., 1992). Since χ^2 depends on the data uncertainties, this procedure would produce unreliable estimates of parameter uncertainty. We modified this procedure by multiplying the χ^2 -estimated parameter uncertainties by the square-root of the reduced χ^2 . This is equivalent to rescaling the data uncertainties such that the reduced χ^2 is unity. This procedure gives statistically correct parameter uncertainties, given ideal data with an undetermined scale factor on the data uncertainties. Although this is certainly not the case here, based on our observations, we believe that this procedure gives better parameter uncertainty estimates than those provided directly by the program.

The poorly-crystalline samples and HexBir were modeled using a structure belonging to the monoclinic $C12/m1$ space group. A model with hexagonal $R\bar{3}M$ symmetry (Gateshki et al., 2004) was also tried but gave poorer fits. The $C12/m1$ group allows for deviations of single-layer symmetry from hexagonal symmetry due to structural distortions. This deviation is evaluated based on the value of a/b which is $\sqrt{3}$ (1.732) for hexagonal symmetry. The $C12/m1$ group also permits the β angle, the stacking vector, to deviate from 90° , corresponding to MnO_6 layer shifts along the a axis relative to each other. This is critical for structures comprised of turbostratically stacked layers as expected in these poorly-crystalline Mn oxide samples. Other Mn oxide standards were not modeled in this study, except for pyrolusite, which was modeled in the $P42/mmm$ space group to obtain the transferable instrumental parameters used for other models.

For models in the $C12/m1$ space group, unit cell parameters and atom positions were varied as allowed by the space group. These include a , b , c and β , and x and z fractional coordinates for the oxygen atoms and IL species. In all cases, OL Mn and O atoms were modeled with atomic anisotropic displacement parameters (ADPs) to account for stacking disorder (Petkov et al., 2002; Masadeh et al., 2007). The off-diagonal ADP allowed by the space group, in this case B_{13} , was determined not to improve the fits significantly. Therefore, it was fixed at zero and not varied. Varying IL anisotropic ADPs caused unreliable convergence, so the IL ADPs were modeled isotropically.

Occupancies of the OL Mn and IL O (i.e., H_2O) were allowed to vary. The IL cation occupancies were linked to the Mn occupancies according to charge balance (Villalobos et al., 2006). We found that this constraint was required for reliable determination of the ADPs. Chemical composition of the poorly-crystalline phases suggest that more than one cation species exists in the IL, but the occupancies of the individual species cannot be determined reliably. Assuming that the parameters of a single IL cation species can capture the scattering effects of all IL cation species, the occupancy constraints are only approximate. A three-to-one ratio between water molecules and the IL cations was also enforced (Villalobos et al., 2006).

For the samples with nanoparticulate sizes (δ - MnO_2 , $PolyMnO_2$ and $BioMnO_x$), the finite CSD size of the particles was modeled as a bulk PDF attenuated by a characteristic function (CF) that is the autocorrelation function of the shape of the nanoparticles (Guinier et al., 1955). Both cylindrical (Guinier et al., 1955) and spheroidal (Lei et al., 2009) CFs were used to model the effect of CSD size (Farrow and Billinge, 2009). Both approaches worked well and gave very similar results. Only the results obtained from a cylindrical shape are reported.

For all fits, the scale and vibrational correlation terms (δ_2) were allowed to vary. The two instrumental resolution parameters, i.e., damping (Q_{damp}) and broadening (Q_{broad}) factors, were fixed in the fits. These parameters ($Q_{damp} = 0.045 \text{ \AA}^{-1}$; $Q_{broad} = 0.069 \text{ \AA}^{-1}$) were derived by fitting the PDF of pyrolusite. R_w values were calculated between $r_{min} = 1 \text{ \AA}$ and $r_{max} = 50 \text{ \AA}$, while fits were performed with $r_{min} = 0 \text{ \AA}$. The r -interval used in the fits is 0.1 \AA , which is smaller than the Nyquist interval (0.126 \AA) for $Q_{max} = 25 \text{ \AA}^{-1}$ (Farrow et al., 2011). Since the layers are stacked along the crystallographic c -axis in these materials, the morphology and internal structure are correlated and the CF formalism in Eq. (1) is not strictly applicable (Gilbert, 2008). As a result of using the CF, the attenuation of the PDF peak intensities may not be adequately modeled (Gilbert, 2008). This has an uncertain effect on the modeled ADPs and site occupancies.

3. RESULTS

3.1. Chemical composition

The chemical composition of the Mn oxide samples and standards are given in Table 1. The chemical composition information was used in the PDF data reductions and also as a reference for composition of structural models in the PDF simulations. The dominant cations associated with Mn oxides are alkaline and alkaline earth metals (Na, K, Mg and Ca) which are introduced from the chemicals used in their syntheses (Table 1). Since the todorokite sample is a naturally-occurring material, it may contain heavy metal impurities whose contents were not measured in this study. These cations are located in the interlayer regions or tunnels of Mn oxides to compensate for positive charge deficiencies. TrBir contains a large amount of Na^+ to compensate for the charge deficiency caused solely by Mn^{3+} substitution for Mn^{4+} in octahedral layers (OL), with

Table 1
Chemical composition of the Mn oxide samples and standards.

	Chemical compositions
Todorokite	$\text{Na}_{0.03}\text{Mg}_{0.09}\text{MnO}_2 \cdot 0.46\text{H}_2\text{O}$
Cryptomelane	$\text{K}_{0.09}\text{MnO}_2 \cdot 0.1\text{H}_2\text{O}$
Pyrolusite	MnO_2^{a}
TrBir	$\text{Na}_{0.29}\text{MnO}_2 \cdot 0.55\text{H}_2\text{O}$
HexBir	$\text{MnO}_2 \cdot 0.56\text{H}_2\text{O}$
AcidBir	$\text{K}_{0.23}\text{MnO}_2 \cdot 0.43\text{H}_2\text{O}$
$\delta\text{-MnO}_2$	$\text{Na}_{0.07}\text{K}_{0.05}\text{MnO}_2 \cdot 0.44\text{H}_2\text{O}$
PolyMnO ₂	$\text{Na}_{0.07}\text{K}_{0.18}\text{MnO}_2 \cdot 0.66\text{H}_2\text{O}$
BioMnO _x ^b	$\text{Mg}_{0.1}\text{Ca}_{0.1}\text{MnO}_2 \cdot y\text{H}_2\text{O}$

^a Not measured.

^b Water contents (*y*) in the BioMnO_x sample cannot be accurately determined due to the presence of bacterial cells.

Mn³⁺ accounting for one third of the Mn (Lanson et al., 2002). For HexBir, the vacant sites are offset by Mn²⁺, Mn³⁺ and H⁺ and therefore, no other metals exist in its interlayer (IL) region. AcidBir and PolyMnO₂ contain similar total amounts of Na and K, which double the amount in $\delta\text{-MnO}_2$. Only Mg and Ca were detected in the BioMnO_x sample, which introduces an equivalent charge of 0.4 per Mn, much higher than in other samples. As mentioned previously, this high amount of Mg and Ca is probably due to desorption of Mg and Ca, originally associated with the surface of the bacterial materials when the chemical composition measurements were made. From the chemical compositions, we cannot tell if IL Mn exists in the structure of AcidBir, $\delta\text{-MnO}_2$, BioMnO_x and PolyMnO₂. The structural water contents (80–250 °C) estimated in this study (Table 1) are less than those previously reported (Villalobos et al., 2006). However, it is hard to specify the temperature range to accurately determine amounts of specific types of structural H₂O. This is particularly the case for materials with large surface area and amorphous structure because multiple water species may exist. In addition, absorbed and interlayer H₂O on the layered structure of nanoparticles might not be distinguishable.

3.2. HRTEM analyses

AcidBir contains large size crystals with multiple stacked layers (Fig. 1b), indicating a bulk material. However, the fringes are not straight, suggesting each single layer has curvature, which may increase layer stacking inconsistencies along the *c*-axis direction ([001]). The multiple stacked layers are rarely observed in $\delta\text{-MnO}_2$, PolyMnO₂ and BioMnO_x (Fig. 1c–h), suggesting that these materials contain a very limited number of poorly stacked layers or are single-sheets of MnO₆ materials. $\delta\text{-MnO}_2$ consists of both crystal and amorphous domains (Fig. 1d) while PolyMnO₂ is comprised of crystals (Fig. 1f). We found that if $\delta\text{-MnO}_2$ is dialyzed, instead of centrifuged after its synthesis for residual solute removal, it contains more amorphous particles. Regardless of the cleaning procedures, PolyMnO₂ was always crystalline (Fig. 1f). The particle size of PolyMnO₂ is ~8–10 nm, estimated from the TEM images (Fig. 1f). Unfortunately, it is hard to delineate boundaries of individ-

ual particles of $\delta\text{-MnO}_2$ for particle size determination (Fig. 1d). Compared to globular aggregates of PolyMnO₂ particles (Fig. 1e), $\delta\text{-MnO}_2$ displays veil-like morphology (Fig. 1c). The BioMnO_x sample appears as fibers surrounding bacterial materials at a larger scale (Fig. 1g). Numerous crystalline domains with irregular shapes and varying size are surrounded by a large amount of amorphous areas (Fig. 1h).

3.3. XRD patterns and reduced structure functions (*F(Q)*)

The XRD pattern of TrBir suggests no or low amounts of crystalline impurities (Fig. 2), such as $\beta\text{-MnOOH}$ and Mn₃O₄, which have strong diffraction peaks at 4.62 and 2.49 Å, respectively. HexBir yields an XRD pattern distinct from that of TrBir due to the migration and/or disproportionation of Mn³⁺ originally in the layers of TrBir to the interlayer region by acidification (Lanson et al., 2000). The reflections around 7.25 and 3.63 Å for HexBir and 7.16 and 3.58 Å for TrBir correspond to the basal plane (001) and (002) reflections. The XRD patterns for $\delta\text{-MnO}_2$ and AcidBir show three broad diffraction peaks at *d*-spacings around 2.41, 1.41 and 1.22 Å, consistent with previous studies (Chukhrov et al., 1980; Villalobos et al., 2003). AcidBir has two extra relatively sharp diffraction peaks around 7.28 and 3.64 Å, corresponding to the basal plane peaks as seen in TrBir and HexBir. PolyMnO₂ has the same set of peaks as $\delta\text{-MnO}_2$, but they are broader. The diffractions in the range 5–15 Å show similar peak shapes and positions but different widths for BioMnO_x, $\delta\text{-MnO}_2$ and PolyMnO₂. Additionally, $\delta\text{-MnO}_2$ has a shoulder around ~7.34 Å. Reduced structure functions (*F(Q)*) (Fig. 2b) reflect hyperfine features (Fig. 2b). These normalized diffraction peaks show similar shapes and positions for HexBir and the four poorly-crystalline samples, which are therefore sharing similar structural features. From HexBir to PolyMnO₂ (from top to bottom), one can observe smaller numbers of diffraction peaks, and these are less sharp and poorly resolved, indicating decreasing particle sizes and/or crystallinity.

3.4. Qualitative analyses of pair distribution functions (*G(r)*)

The poorly-crystalline Mn oxide samples have similar features in *G(r)* at low *r* with HexBir, TrBir, cryptomelane and todorokite, although the intensities are different (Fig. 2c). This indicates that these materials share similar local structure, which is edge-sharing linkage of Mn octahedra. At higher *r*, the *G(r)* of the poorly-crystalline samples resemble that of HexBir only (Fig. 2c), i.e., sharing more common structural features with HexBir. This suggests that they are neither tunnel structures, such as todorokite, nor the layered structures having a TrBir-like structure. The falloffs in the intensity of structural features with increasing *r* are more pronounced for the poorly-crystalline samples (Fig. 2c), reflecting their nanoparticulate sizes. Note that all PDFs demonstrate a gradual falloff due to resolution effects from the experimental setup (Toby and Egami, 1992).

The first major peaks at ~1.90 Å in *G(r)* correspond to Mn–O correlations in the first O coordination shell of Mn

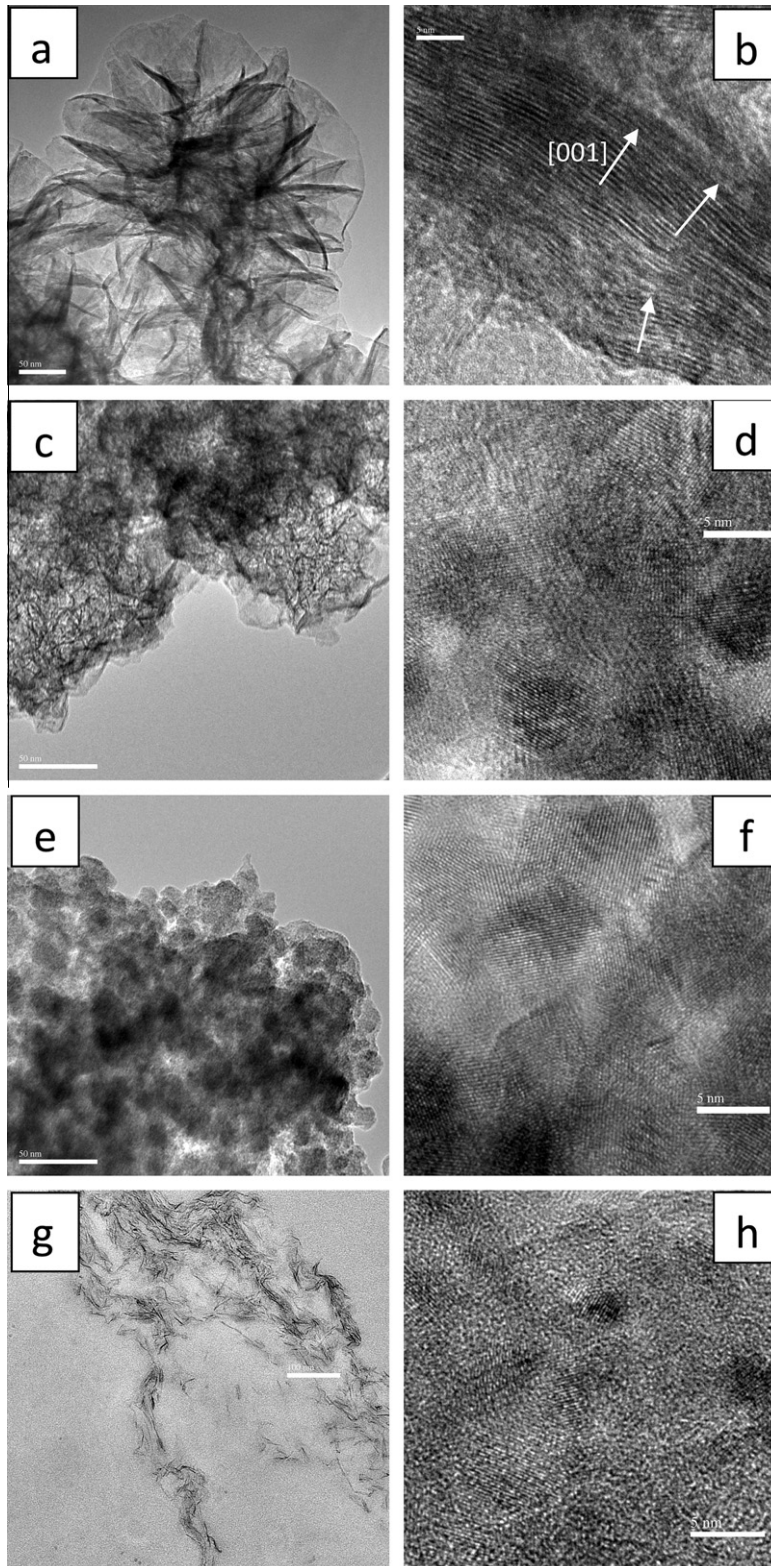


Fig. 1. HR-TEM images of Mn oxide samples: AcidBir, (a and b); δ -MnO₂, (c and d); PolyMnO₂, (e and f) and BioMnO_x, (g and h). The image, (g), was collected from an unstained microtome section; and the image, (h), was directly collected from the BioMnO_x sample without any pretreatment. The scale bars for a, c, e, g and b, d, f, h are 50 nm and 5 nm, respectively. The arrows in (b) indicate the crystal direction of [001].

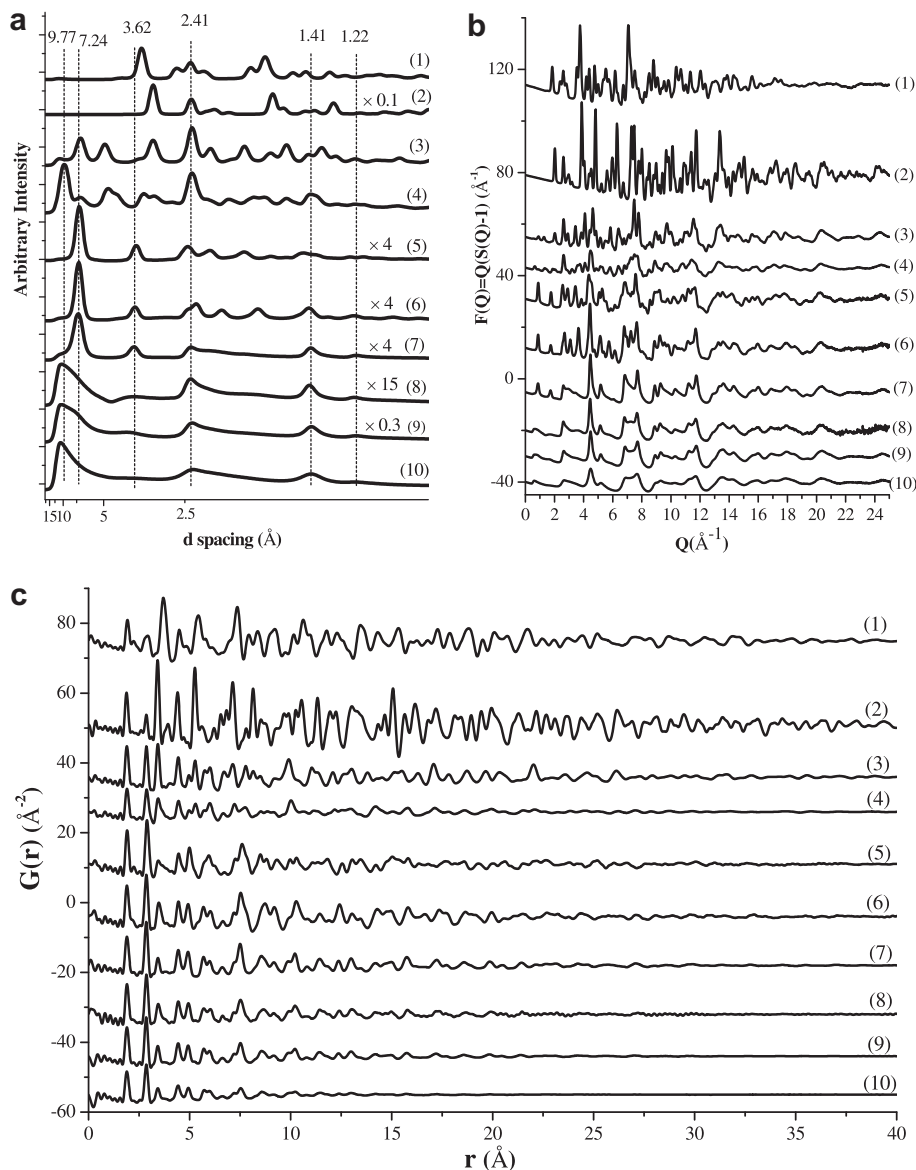


Fig. 2. X-ray diffraction patterns (a), reduced structure functions (b) and PDFs (c) of Mn oxide samples. (1) γ -MnOOH, (2) pyrolusite, (3) cryptomelane, (4) todorokite, (5) TrBir, (6) HexBir, (7) AcidBir, (8) BioMnO_x, (9) δ -MnO₂, and (10) PolyMnO₂. The intensities of XRD patterns (a) were adjusted by multiplying certain folds for convenient comparisons between samples in the same scale.

(Fig. 3a). The peak (1.917 Å) for γ -MnOOH is at longer r than for the other samples (Table 2); this peak is highly asymmetric and has a shoulder peak at 2.24 Å. The Mn–O peak of pyrolusite is at shorter r (1.876 Å, Table 2), more symmetric (Fig. 2a), and the shoulder peak is very weak. Both pyrolusite (Mn⁴⁺) and γ -MnOOH (Mn³⁺) are 1 × 1 tunnel structures but differ in Mn oxidation states. Mn³⁺ octahedra exhibit strong Jahn–Teller distortion and the longer Mn–OH bond further distorts the Mn³⁺ octahedra. This has been clearly seen in PDF measurements of perovskite managanites with Mn³⁺ (Qiu et al., 2005). The peak at 1.917 Å corresponds to the average of the four equatorial Mn–O bond distances while the two axial Mn–O bonds contribute to the shoulder peak at 2.24 Å.

TrBir has an obviously asymmetric Mn–O peak at 1.904 Å and a shoulder peak at ~2.24 Å. Compared to TrBir, the Mn–O peaks of δ -MnO₂, AcidBir and PolyMnO₂ are symmetric and at shorter r (1.891–1.895 Å) with less pronounced shoulder peaks at 2.24 Å. It is known that these three Mn oxides contain little or no Mn²⁺ and Mn³⁺ while Mn³⁺ accounts for one third of Mn positions in TrBir. Therefore, the Mn–O peak shoulder in TrBir is also likely due to the Mn³⁺ octahedral distortion as observed in γ -MnOOH. Correlations between interlayer Na⁺ and K⁺ and their coordinated O atoms do not significantly contribute to the shoulder peaks, as seen in AcidBir and PolyMnO₂, because of the longer Na–O and K–O bond distances (>2.3 Å) and weaker Na/K X-ray scattering strength

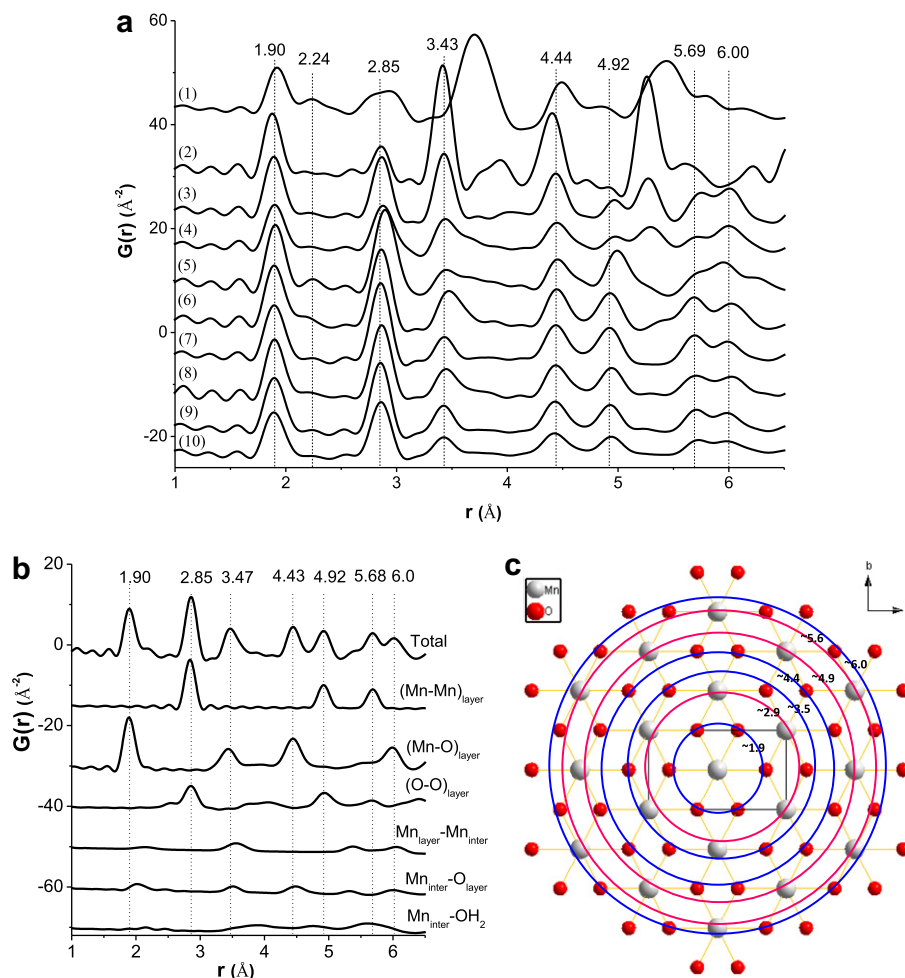


Fig. 3. $G(r)$ within 6.5 Å for closer examination of local atomic correlations, (a), calculated major atomic correlations of HexBir, (b) and a top view of its single-layer structure, (c). Labels in (a) are the same as those in Fig. 2.

Table 2

Positions, amplitude (Am.) and width (Wd.) of the first and second major peaks at ~ 1.90 and ~ 2.85 Å obtained from peak fitting with Gaussian functions.

	r (Å)	Am. (Å ⁻²)	Wd. (Å)	r (Å)	Am. (Å ⁻²)	Wd. (Å)
TrBir	1.904	12.17	0.181	2.896	15.97	0.217
HexBir	1.893	9.96	0.178	2.864	14.04	0.189
AcidBir	1.895	9.54	0.191	2.858	15.07	0.197
δ -MnO ₂	1.895	9.76	0.194	2.856	14.32	0.197
PolyMnO ₂	1.891	8.10	0.197	2.861	10.70	0.200
BioMnO _x	1.893	10.08	0.178	2.864	13.99	0.195
Pyrolusite	1.876	11.04	0.168	2.865	6.00	0.154
Cryptomelane	1.891	10.73	0.181	2.867	11.41	0.181
Todorokite	1.898	7.92	0.180	2.880	8.96	0.220
γ -MnOOH	1.917	7.70	0.180	–	–	–

compared to Mn (Lanson et al., 2002; Rustad et al., 2003; Gaillot et al., 2007). Asymmetric Mn–O peaks at 1.893 Å and relatively apparent shoulder peaks are also observed for HexBir (2.20 Å) and BioMnO_x (2.24 Å). The two materials can contain significant Mn³⁺ and Mn²⁺ in MnO₆ layers (Mn³⁺) and interlayers (Mn^{2,3+}) (Silvester et al., 1997; Zhu et al., 2010a). Mn²⁺–O(H₂) bond length is ~ 2.17 Å

(Bock et al., 1999) and therefore, the presence of Mn²⁺ can also destroy the Mn–O peak asymmetry, which results in the shoulder peaks in addition to Mn³⁺. Mg²⁺ ($d_{\text{Mg-O}} = \sim 2.10$ Å) (Bock et al., 1999) could also contribute to the asymmetry of the Mn–O peak in BioMnO_x, but due to its weak scattering ability, this contribution is insignificant. The observed shoulder peak at 2.20 Å in BioMnO_x is

probably not due to Ca^{2+} because of its longer bond length ($d_{\text{Ca-O}} = \sim 2.4 \text{ \AA}$) (Bock et al., 1999).

The peaks at $\sim 2.85 \text{ \AA}$ are dominated by Mn–Mn and O–O (bridged O) correlations in two edge-sharing Mn octahedra (Fig. 3b). The peak displayed at longer r for TrBir (2.896 \AA) than for the other samples is caused by the presence of Mn^{3+} in TrBir (Lanson et al., 2002). The peaks for BioMnO_x and HexBir are at a slightly longer r than AcidBir, δ -MnO₂ and PolyMnO₂ (Fig. 3a and Table 2). Adsorption of heavy metals on vacant sites of layered Mn oxides may not alter the $\sim 2.85 \text{ \AA}$ peak position. Therefore, these slightly longer Mn–Mn and O–O distances are due to the presence of Mn^{3+} in the Mn layers (Webb et al., 2005a). Adsorption of $\text{Mn}^{2/3+}$ on vacant sites results in a $\sim 3.50 \text{ \AA}$ Mn_{OL}–Mn_{IL} correlation (Silvester et al., 1997), which can contribute to the right shifts of the peaks at 3.43 \AA for HexBir and BioMnO_x (Fig. 3a and b).

Other pair correlation contributions at 4.44, 4.92, 5.69 and 6.00 \AA are more complex. For layered Mn oxides, these peaks mainly result from correlations within a single Mn layer (Fig. 3b and c). Other correlations involving IL species modify these peaks (Fig. 3a). These can be better assessed through quantitative modeling.

For tunnel Mn oxides, corner-sharing Mn–Mn correlations in the structural frames also contribute to the peak at 3.43 \AA , in addition to Mn–O correlation at similar distance. The intensity of the Mn peaks at 2.85 \AA relative to those at 3.43 \AA partially reflects the proportions of these two linkages. As the tunnel size decreases from TrBir to todorokite (3 × 3), cryptomelane (2 × 2) and to pyrolusite (1 × 1), the amplitude ratio of the 3.43 \AA to the 2.85 \AA peaks increases because components of corner-sharing Mn–Mn correlations become more dominant with the decreasing tunnel size (Fig. 3a).

3.5. Modeling pair distribution functions ($G(r)$)

The R_w values from the PDF models indicate acceptable agreement between simulated $G(r)$ and experimental data (Fig. 4), given such big $r_{\text{max}} = 50 \text{ \AA}$. However, relatively large discrepancies in the region of $2.5 < r < 5 \text{ \AA}$, particularly around the second ($\sim 2.85 \text{ \AA}$) and third peak ($\sim 3.43 \text{ \AA}$), were observed for all fits except for PolyMnO₂. The R_w value is lower for PolyMnO₂, primarily because the oscillations are negligible past 25 \AA , and therefore are fit quite well by the CF-attenuated model PDF.

3.5.1. HexBir

The reported model for HexBir contains vacant sites which are capped by IL $\text{Mn}^{2/3+}$ on either side (Silvester et al., 1997). Thus, the Occ_{MnOL} is correlated with Occ_{MnIL} as $\text{Occ}_{\text{MnIL}} = 1 - \text{Occ}_{\text{MnOL}}$ in the fitting model, assuming that each vacant site is covered by one $\text{Mn}^{2,3+}$ for HexBir at pH 5 (Lanson et al., 2000). The obtained unit-cell parameters and atomic fractional coordinates are listed in Tables 3 and 4, and the fit is shown in Fig. 4. The calculated major interatomic distances from the optimal model are listed in Table 5. The value of a/b (1.737) is very close to $\sqrt{3}$, indicating hexagonal layer symmetry, consistent with previous studies (Drits et al., 1997; Lanson et al., 2000). We note that

U_{11} (0.01 \AA^2) for O_{OL} atoms in HexBir is significantly larger than those (0.003–0.005 \AA^2) in the other four samples (Table 4), indicating greater structural disorder of O_{OL}. The enlarged atomic displacement parameters is presumably caused by the presence of a Jahn–Teller distortion of $\text{Mn}_{\text{OL}}^{3+}$ (Billinge et al., 1996; Bozin et al., 2007) present in HexBir, but not in the other samples where almost all the Mn ions are in the 4+ state. The calculated 001 d-spacing is 7.227 \AA ($c \cdot \sin \beta$), in good agreement with the experimental observation, $\sim 7.22 \text{ \AA}$ (Fig. 2a). The stacking vector (β), 91.17°, deviates from 90°, indicating a slight layer shift along the opposite direction of the crystallographic a -axis. The large value ($U_{33} = 0.100$) of the Mn ADP in the c -axis direction indicates a stacking disorder (Petkov et al., 2002; Gateshki et al., 2004), which may be inherited from the disordered stacking in its precursor (TrBir) (Yang and Wang, 2002). The refined occupancy factors for the layer Mn ($\text{Occ}_{\text{MnOL}} = 0.770$) and interlayer Mn ($\text{Occ}_{\text{MnIL}} = 0.230$) slightly deviate from those reported in previous studies [0.833 and 0.167, respectively] (Silvester et al., 1997; Lanson et al., 2000). The Mn_{IL} was almost above or below the Mn_{OL} at a distance of 3.499–3.608 \AA (Table 5) from the nearest Mn_{OL}, with an average value of 3.552 \AA . This is consistent with the EXAFS spectroscopic determination (3.542 \AA) (Silvester et al., 1997). The water content, 0.69, is higher than the result obtained from TGA analysis (Table 1).

3.5.2. AcidBir, δ -MnO₂, PolyMnO₂ and BioMnO_x

In order to reduce the number of fitting variables, K^+ is assumed to be the only IL cation for δ -MnO₂, PolyMnO₂ and AcidBir, although Na^+ is also present (Table 1). Inclusion of IL Mn in addition to K^+ was tested and did not improve the goodness of fits for these materials. This suggests that Mn_{IL} amounts are low or not high enough to be reliably detected by PDF analysis. This is consistent with their Mn–O peak positions and symmetry. Inclusion of both Ca and Mn as IL cations for BioMnO_x resulted in unreliable convergences, likely because they have similar positions. Thus, Ca was applied in the fitting for BioMnO_x but represents both Mn and Ca. It is assumed that one vacant site corresponds to 4K^+ or 2Ca^{2+} (Villalobos et al., 2006; Post et al., 2008).

Inclusion of the particle size and shape parameters in the fit does not improve the goodness of fit for AcidBir, indicating that the AcidBir structure has long-range order, which is consistent with its TEM image. The other three nanoparticulate samples have relatively large lateral dimensions but very thin thicknesses, i.e., resembling disks. Although not determined accurately, particularly for the lateral dimensions, both lateral and c -axis dimensions generally decrease from BioMnO_x to δ -MnO₂ and to PolyMnO₂. Based on the 001 d-spacing values, their CSDs contain 1–3 stacked MnO₆ layers. The perpendicular CSD dimension of δ -MnO₂ agrees well with reported values (10 \AA) based on XRD simulations (Villalobos et al., 2006; Grangeon et al., 2009). The stacking vectors (β), greater than 90° by 5.7°–9.0°, imply substantial layer shifts along the opposite direction of the a -axis compared to HexBir. The huge Mn ADP values (U_{33}) in the c -axis direction suggest severe

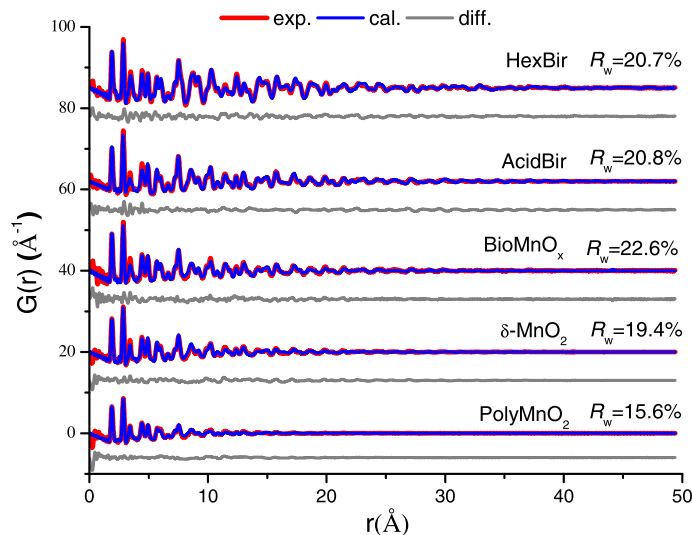


Fig. 4. Comparison between experimental (blue) and calculated (red) PDFs for the Mn oxides. The gray lines are the differences between experimental and calculated PDFs. R_w is the fitting goodness for each Mn oxide. Structural parameters used for calculations are listed in Tables 3 and 4. (For interpretation of the references to colour in this figure legend, the reader is referred to the web version of this article.)

Table 3

Unit cell and atom-independent parameters from SrFit with $r_{\max} = 50$ Å. The parameters *thickness* and *diameter* refer to the dimensions of the cylindrical domain size, where applicable (cf. Fig. 4).

Unit cell	HexBir	AcidBir	BioMnO _x	δ-MnO ₂	PolyMnO ₂
a (Å)	4.935(5)	4.942(5)	4.950(6)	4.966(6)	4.966(2)
b (Å)	2.841(2)	2.829(3)	2.834(3)	2.825(3)	2.8409(14)
a/b	1.737(2)	1.747(2)	1.746(3)	1.758(3)	1.7587(12)
c (Å)	7.230(6)	7.32(4)	7.20 ^a	7.35(2)	7.20 ^a
β	91.17(14)	96.0(2)	99.0(3)	95.7(2)	97.48(8)
δ_2	3.40(13)	3.45(2)	3.46(3)	3.34(5)	3.32(5)
Scale	1.50(3)	1.27(2)	1.57(6)	1.40(3)	1.40(4)
Thickness(Å)	–	–	14(2)	10.0(13)	7.1(8)
Diameter(Å)	–	–	>50	>40	26(5)
R_w (%)	20.7	20.8	22.6	19.4	15.6

^a Due to the not well correlated layers, the c lattice spacing could not be refined with certainty and was fixed at this value.

stacking disorders in these materials (Petkov et al., 2002; Gateshki et al., 2004).

The refined a values for the poorly-crystalline samples are larger while the b values are smaller than those of HexBir (Table 3), resulting in a/b values larger than $\sqrt{3}$ and suggesting significant deviations from hexagonal layer symmetry. These deviations increase from HexBir, to AcidBir and BioMnO_x, and to δ-MnO₂ and PolyMnO₂. The a values also increase in this order but b values exhibit no trends. For AcidBir, the calculated 001 d-spacing, 7.28 Å ($c \cdot \sin(\beta)$), agrees with the experimental observation (~ 7.28 Å) from the XRD pattern (Fig. 2). The refined 001 d-spacings are 7.111, 7.312 and 7.139 Å for BioMnO_x, δ-MnO₂ and PolyMnO₂, respectively; however, 001 d-spacings are not obvious from the XRD patterns. Even so, the broad shoulder around ~ 7.34 Å in the δ-MnO₂ XRD pattern has been assigned as the 001 d-spacing (Grangeon et al., 2009). Our calculated 001 d-spacing (7.312 Å) for δ-MnO₂ supports this viewpoint.

The c value was fixed at 7.20 Å for BioMnO_x during the fit (Villalobos et al., 2006). Otherwise, it results in a c value of 6.93 Å, corresponding to a d-spacing of 6.85 Å (Supporting information). A d-spacing smaller than 7 Å is unlikely for layered Mn oxides unless they are dried at high temperature (Chen et al., 1996). However, Gateshki et al. (2004) obtained a smaller (6.43 Å) 001 d-spacing for a hydrous layered Mn oxide sample synthesized by KMnO₄ reduction by LiI. The c value for PolyMnO₂ was also fixed at 7.20 Å due to its large uncertainty during the fit. The parameters obtained with freely-floated c values are reported in the supporting information.

The BioMnO_x sample has the lowest Occ_{MnOL} (0.847) among the four poorly-crystalline samples. The other three have similar Occ_{MnOL} which are higher than that of the BioMnO_x sample by 0.083–0.089. The interlayer cation contents per Mn_{OL} obtained from modeling (Table 4) for AcidBir and PolyMnO₂ are 0.044 and 0.028 higher, respectively, than their corresponding chemical compositions

Table 4

Atom parameters from SrFit with $r_{\max} = 50 \text{ \AA}$. x , y and z are fractional coordinates and the ADPs are in units of \AA^2 . Errors are in parentheses (cf. Fig. 4).

	x	y	z	U_{iso} or U_{11}	U_{22}	U_{33}	Occ. ^a	Occ. ^{1,b}	BVS ^c
<i>HexBir</i>									
Mn _{OL}	0	0	0	0.0030(11)	0.0028(11)	0.100(6)	0.769(8)	1	4.0
O _{OL}	0.3600(10)	0	0.1338(6)	0.01 (2)	0.0029(10)	0.0021(7)	2	2.60	–
Mn _{IL}	0.993(4)	0	0.294(2)	0.0047(12)	–	–	0.230(8)	0.299	–
O _{IL}	0.714(7)	0	0.472(4)	0.010(2)	–	–	0.69(2)	0.897	–
<i>AcidBir</i>									
Mn _{OL}	0	0	0	0.011(9)	0.0029(5)	0.27(3)	0.936(4)	1	4.05
O _{OL}	0.349(2)	0	0.1314(10)	0.005(2)	0.007 (2)	0.11(2)	2	2.138	–
K _{IL}	0.112(10)	0	0.556(10)	0.009(6)	–	–	0.256(14)	0.274	–
O _{IL}	0.521(11)	0	0.553(10)	0.019(9)	–	–	0.768(4)	0.821	–
<i>BioMnO_x</i>									
Mn _{OL}	0	0	0	0.00(2)	0.0028(7)	0.23(3)	0.847(8)	1	3.96
O _{OL}	0.358(2)	0	0.1360(9)	0.0026 (11)	0.004(2)	0.08 (2)	2	2.361	–
(Ca/Mn/Mg) _{IL}	0.983(4)	0	0.451(4)	0.0007(6)	–	–	0.31(2)	0.361	–
O _{IL}	0.602(5)	0	0.557(6)	0.006(3)	–	–	0.92(3)	1.08	–
<i>δ-MnO₂</i>									
Mn _{OL}	0	0	0	0.002(2)	0.0035(14)	0.21(3)	0.930(4)	1	4.01
O _{OL}	0.344(2)	0	0.1311(9)	0.003(2)	0.002(2)	0.011(3)	2	2.151	–
(K/Na) _{IL}	0.116(4)	0	0.546(4)	0.002(2)	–	–	0.280(14)	0.301	–
O _{IL}	0.505(5)	0	0.536(3)	0.0010(10)	–	–	0.84(4)	0.903	–
<i>PolyMnO₂</i>									
Mn _{OL}	0	0	0	0.004(4)	0.005(4)	0.05(2)	0.935(5)	1	4.06
O _{OL}	0.3451(10)	0	0.1322(10)	0.003(5)	0.002(4)	0.10(4)	2	2.139	–
(K/Na) _{IL}	0.0547(6)	0	0.5779(6)	0.00005(7)	–	–	0.26(2)	0.278	–
O _{IL}	0.501(7)	0	0.552(5)	0.004(5)	–	–	0.78(6)	0.833	–

^a Occupancies for interlayer species may be overestimated.

^b Occupancies per Mn_{OL}.

^c Bond valence sum (BVS) analyses based on $s = \exp((R_0 - R)/B)$, in which $R_0 = 1.753$ (Mn⁴⁺), $B = 0.37$, and R is the Mn–O bond length (Brown and Altermatt, 1985).

(Table 1). For δ -MnO₂, however, the modeling result is more than two times higher than the chemical composition. In terms of interlayer H₂O, the contents are significantly overestimated by the modeling compared to the TGA measurements.

3.6. Bond valence analyses

In order to examine whether the refined structure is chemically reasonable, bond valence sum (BVS) analyses (Brown and Altermatt, 1985) were performed for Mn_{OL} (Table 4). The BVS method is complicated and is still in development for bond valence analyses at solid-water interfaces (Brown, 2009), relevant for the IL species in these samples, and therefore, BVSs for IL cation species were not calculated. The BVSs for Mn_{OL} range from 3.96 to 4.06 for the four samples, which are very close to the formal oxidation state of 4 for Mn, validating the refined crystal structure for these nanomaterials. The BVS value of HexBir is also calculated to be 4.0, although in this case we expect the presence of Mn³⁺ on around 0.111 of the sites and the average Mn oxidation state should be smaller than 4 (Lanson et al., 2000). However, the structural model used does not have distinct crystallographic sites for the 3+ and 4+ Mn ions and the calculated BVS value is not expected to

be accurate in this case. As discussed above, the presence of the Mn³⁺ results in enlarged U_{iso} on the neighboring oxygen sites, rather than changing the *average* bond lengths in a way that would reduce the calculated BVSs.

4. DISCUSSION

The PDF analyses provide direct structural information for the poorly-crystalline Mn oxides studied here. PDFs list atomic pair correlations up to several nanometers which are much more extensive, and subsequently more convincing, than radial structure functions derived from EXAFS spectroscopy, which are valid only up to 0.6 nm. Comparisons of the PDFs of these samples with Mn oxide standards unambiguously indicate that these materials are layered structures. This conclusion is further corroborated by the successful model fittings with layered structural models belonging to the *C12/m1* space group. A generic structure model is depicted in Fig. 5.

4.1. Fitting accuracy

Relatively large mismatches, which reflects local structure, between calculated and experimental PDFs (except PolyMnO₂) are observed in the r range within 5 Å. The

Table 5

Calculated interatomic distances (Å) using the optimum structural parameters listed in Tables 3 and 4. The numbers in parentheses are averaged values.

Atomic pairs	HexBir	AcidBir	BioMnO _x	δ-MnO ₂	PolyMnO ₂
(Mn–O) _{OL}	1.860 × 4, 2.006 × 2 (1.909)	1.906 × 4, 1.885 × 2 (1.899)	1.917 × 4 1.886 × 2 (1.907)	1.916 × 4 1.876 × 2 (1.903)	1.925 × 4 1.849 × 2 (1.900)
(Mn–Mn) _{OL}	2.847 × 4, 2.841 × 2 (2.845)	2.847 × 4, 2.829 × 2 (2.841)	2.852 × 4, 2.834 × 2 (2.846)	2.857 × 4, 2.825 × 2 (2.846)	2.861 × 4, 2.841 × 2 (2.854)
(Mn/Ca) _{IL} -Mn _{OL}	3.499 × 2, 3.549 × 2, 3.608 × 2 (3.552)	–	3.980 × 2 4.321 × 2 4.659 × 2 (4.32)	–	–
(Mn/Ca) _{IL} -O _{OL}	1.939 × 2, 2.170 (2.016)	–	2.664 × 2 3.148 (2.826)	–	–
Mn _{IL} -H ₂ O	2.192 × 2, 1.904 (2.096)	–	–	–	–
Na/K-O _{OL}	–	2.680 × 2 3.325 3.394 (3.020)	–	2.752 × 2, 3.400 3.454 (3.090)	2.520 × 2, 3.562 3.409 (3.003)
H ₂ O-O _{OLnext}	2.9306 × 2 2.9760 (2.946)	2.332	2.188	2.487	2.303

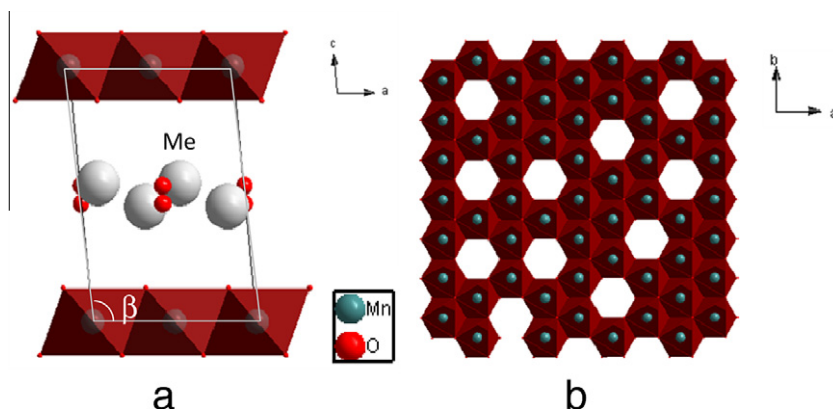


Fig. 5. A generic structure model for layered Mn oxides (a) and a Mn octahedral layer with vacant sites (b). The large white balls (Me) represent alkaline and alkaline earth metals and the small red balls are oxygen atoms representing H₂O molecules. The vacant site density and positions in (b) are arbitrary. (For interpretation of the references to colour in this figure legend, the reader is referred to the web version of this article.)

discrepancies are pronounced when comparing the measured Mn–O/Mn distances (Table 2) to the calculated values based on the optimized crystal structures (Table 5). Derived structures from PDF modeling relied on the r range over which a fit is performed. A longer fitted r range, emphasizing more of an average structure, may not be the same as a structure obtained over a shorter r range, which reflects more of the local structure. The observed mismatch within 5 Å indicates that the local structure cannot be fully represented by the average structure, obtained from fitting over 50 Å. This could be caused by local distortions which may occur around Mn vacant sites and/or on sheet edges. However, the mismatch within 5 Å is very subtle for Poly-

MnO₂, which is simply due to its sufficiently small particle size compared to other samples. In this case, the coherence length of the local distortions is on the order of the particle size. That is, the smaller particles consist of one or few structural domains and, therefore, the local and average structures are the same.

4.2. Stacking disorder

The huge U_{33} values for Mn and O in the Mn layers suggest that the materials are highly disordered in the stacking direction and the structural models used are incapable of fully capturing the structure in this direction (Petkov

et al., 2002). Nevertheless, the calculated 001 d-spacing from the optimized structural models agree well with the direct measurements from XRD patterns for which experimental 001 d-spacing are available, i.e., HexBir, AcidBir, and even for δ -MnO₂. This suggests that the structural models indeed capture the primary characteristics of the disordered stacking, although not fully. The d-spacing in the poorly-crystalline materials may not be monodisperse and is more likely to have a distribution; therefore, the obtained optimal 001 d-spacings correspond to mean values.

However, this corroboration of a fit using the 001 d-spacing is not applicable to BioMnO_x and PolyMnO₂ due to the absence of the 001 d-spacing. In these two materials, layers are probably less correlated than in other samples, i.e., more disordered in the *c* direction. If layers are not correlated at all, it indicates that it is a single sheet material. PolyMnO₂ is very likely a single sheet material considering the very small size (7.1 Å) in the perpendicular direction (Table 3).

It is generally believed that IL species have larger position disorder than OL species. However, the obtained ADPs are smaller for the IL species than for Mn and O in OL (Table 4). This contradiction can be due to ADPs tending to compensate for the fitting discrepancy caused by possible systematic errors, such as incorrectly determined occupancies, imperfect data correction, inaccuracy of structural models used, etc. It is also possible that stacking disorder might result in relative positional variations for the Mn that give rise to a large ADP.

4.3. Atomic occupancies

To the authors' knowledge, there has not been an approach to directly and accurately determine Occ_{MnOL}, although this quantity may be roughly estimated by assuming metal saturated sorption (Zhu et al., 2010b). Even so, Occ_{MnOL} has been estimated through trial-and-error XRD modeling and EXAFS spectroscopy (Webb et al., 2005a; Villalobos et al., 2006; Bargar et al., 2009). The Occ_{MnOL} values for BioMnO_x and δ -MnO₂ in this study agree well with those obtained by XRD modeling (Villalobos et al., 2006). However, the Occ_{MnOL} of AcidBir is larger than that obtained by Villalobos et al. (2006), which may be due to the difference in the samples used, in addition to the systematic errors of the two approaches. Compared to XRD and PDF modeling, EXAFS multiple-scattering (MS) fitting (Webb et al., 2005a) yielded a much smaller Occ_{MnOL} (0.77(9)) with large uncertainties (~10%) for δ -MnO₂. The smaller value can result from the nanoscale size of δ -MnO₂, which reduces the number of scattering paths between Mn atoms (i.e., edge effects) (Webb et al., 2005a; Bargar et al., 2009). The particle size effects have been considered in the XRD and PDF modeling.

The cation sorption capacity of layered Mn oxides reflects Occ_{MnOL} for layered Mn oxides when: (1) the charge deficiency is only due to vacancies regardless of Mn³⁺; and (2) the charge deficiency is compensated only by metals, i.e., all vacancies are saturated by metals. If metal cations are partially replaced by H⁺ for charge compensation, the Occ_{MnOL} (vacancy contents) based on sorbed metal con-

tents will be overestimated (underestimated). The saturation sorption may be achieved under relatively high pH conditions and high metal concentrations. However, the Mn oxides prepared in this study were not treated in this way to ensure saturated sorption of interlayer cations; therefore, the relations used for interlayer cation contents and Occ_{MnOL} in the PDF modeling may be inappropriate. However, our estimated Occ_{MnOL} might not be affected much because Mn X-ray scattering strength is much higher than for those interlayer cations and therefore, the PDFs are more sensitive to Occ_{MnOL} than the Occ. of alkaline metals. This could be the reason why interlayer cation contents of AcidBir, δ -MnO₂ and PolyMnO₂, particularly for δ -MnO₂, are overestimated. Accordingly, the interlayer water contents are overestimated due to the three-time relation with interlayer cation contents. In addition, interlayer H₂O molecules are spatially close to the alkaline cations, which may contribute to the uncertainties in determined positions and quantities of the alkaline cations.

Mn occupancy in BioMnO_x is significantly lower than in the other three poorly-crystalline Mn oxide samples. This suggests that BioMnO_x formed in the natural environment may be enriched in vacant sites, thereby providing an extraordinary capacity for metal sorption. Interestingly, all of the other three Mn oxide samples have almost the same Mn occupancies (~0.93), probably implying that the Occ. of 0.93 is the characteristic vacant site quantity in laboratory synthesized poorly-crystalline Mn(IV) oxides using wet chemistry.

4.4. Layer symmetry

The poorly-crystalline Mn oxides used in this study were thought to have hexagonal MnO₆ layer symmetry based on the evidence that the XRD diffraction peaks of d-spacing at 1.41 Å are neither split nor asymmetric (Webb et al., 2005a; Drits et al., 2007). However, our results indicate that the average structure of these Mn oxides deviates significantly from this symmetry. The PDF contains additional information from the high-*Q* scattering, which gives better real-space resolution than low-*Q* data, and facilitates the detection of lower than hexagonal symmetry of the structure. It is still not clear what structural/morphological characteristics specifically lead to these deviations. They can be due to particle size effects of nanoparticles (Zhang et al., 2009) given that δ -MnO₂ and PolyMnO₂ have the largest deviations. The presence of Mn vacant sites in MnO₆ layers can also alter layer strains and accordingly layer distortion and symmetry. Furthermore, interactions between interlayer cations and MnO₆ layers at vacant sites may change the layer symmetry, considering that a single MnO₆ layer is very thin. The impact of alkaline metals, heavy metals and H⁺ on layer symmetry is probably different because of their different sorption mechanisms and forces with the layers. Finally, Mn³⁺ in MnO₆ layers can be another factor, although Mn³⁺ amounts in AcidBir- δ -MnO₂ and PolyMnO₂ are minor (Lanson et al., 2002). Studies screening these impacts on the layer symmetry are ongoing.

Petkov et al. (2009) reported a triclinic layered structure for BioMnO_x produced by the bacterium *L. discophora*

SP-6. The Mn-oxidizing bacterium used in this study is different from that of Petkov et al. (2009), but it also produced a layered type of BioMnO_x, probably indicating that the layered type is the structural characteristic of bacterial BioMnO_x compared to the tunnel type produced by the fungus *Acremonium strictum* KR21-2 (Petkov et al., 2009). However, some derived Mn–Mn (2.60 Å) and Mn–O (1.74–1.77 Å) atomic distances within MnO₆ layers based on the Petkov et al. (2009) triclinic layered structure model are too short to be realistic. The model presented here is more in line with expected values (Table 5).

5. CONCLUSIONS

More constrained crystal structures of four poorly-crystalline Mn oxides, including a biogenic Mn oxide sample produced by the bacterium *P. putida* GB-1, were determined using atomic pair distribution function (PDF) analysis. The PDF analyses indicate that these Mn oxides are layered materials with the *C12/m1* crystallographic space group, verifying the prevailing viewpoint that these oxides have a layered structure. The *C12/m1* space group provides more structural variations, required for correctly describing poorly stacked layered materials. The MnO₆ layers contain various amounts of cation vacant sites that have been quantified in the PDF modeling in a reliable manner. The most interesting findings from this study are that the single layer symmetry significantly deviates from the hexagonal, and that adjacent MnO₆ layers substantially shift from each other. Previous researchers were not aware of or unable to quantify these results based on XRD simulation and XAFS analysis. These deviations are probably due to the combination effects of nanometer particle size, presence of Mn vacant sites and adsorption of cations (H⁺ and metals) on vacant sites. One of the limitations of this study is not being able to accurately determine occupancies and positions of light interlayer species (Na⁺, K⁺, Ca²⁺, Mg²⁺ and H₂O molecules). Overall, the results of this study provide insights into the crystal structure of the poorly-crystalline Mn oxides, which is useful for studies regarding their properties in the environment and in industrial applications.

ACKNOWLEDGEMENTS

The authors would like to thank beamline scientists, Dr. Karina W. Chapman, Dr. Peter J. Chupas and Kevin A. Beyer at beamline 11-ID-B at the Advanced Photon Source (APS) and Dr. Jonathan Hanson, Dr. Laura Barrio-Pliego and Dr. Gong Zhang at beamline X7B at the National Synchrotron Light Source (NSLS) for their technical assistance with data collection and analyses. Use of the NSLS was supported by the U.S. Department of Energy, Office of Science, Office of Basic Energy Sciences, under Contract No. DEAC02-98CH10886. The Advanced Photon Source is supported by the Director, Office of Science, Office of Basic Energy Sciences, of the U.S. Department of Energy under Contract No. DEAC02-05CH11231. This publication was made possible by National Science Foundation EPSCoR Grant No. EPS-0814251 and the State of Delaware, and National Science Foundation EAR Grant No. 0544246. Work in the Billinge group was supported by NSF grant DMR-0703940. We are also grateful to Prof. Xionghan Feng at

Huazhong Agricultural University, China, for providing the cryptomelane sample and helpful discussion on the Mn oxide syntheses. The authors also thank Prof. Alexandra Navrotsky at the University of California-Davis for her comments during the manuscript preparation.

APPENDIX A. SUPPLEMENTARY DATA

Supplementary data associated with this article can be found, in the online version, at [doi:10.1016/j.gca.2011.12.006](https://doi.org/10.1016/j.gca.2011.12.006).

REFERENCES

- Bargar J. R., Fuller C. C., Marcus M. A., Brearley A. J., Rosa M. P. D. I., Webb S. M. and Caldwell W. A. (2009) Structural characterization of terrestrial microbial Mn oxides from Pinal Creek, AZ. *Geochim. Cosmochim. Acta* **73**, 889–910.
- Bevington P. R., Robinson D. K. and Bunce G. (1992) *Data Reduction and Error Analysis for the Physical Sciences*. McGraw-Hill, New York.
- Billinge S. J. L. and Levin I. (2007) The problem with determining atomic structure at the nanoscale. *Science* **316**, 561–565.
- Billinge S. J. L., DiFrancesco R. G., Kwei G. H., Neumeier J. J. and Thompson J. D. (1996) Direct observation of lattice polaron formation in the local structure of La_{1-x}Ca_xMnO₃. *Phys. Rev. Lett.* **77**, 715–718.
- Bock C. W., Katz A. K., Markham G. D. and Glusker J. P. (1999) Manganese as a replacement for magnesium and zinc: functional comparison of the divalent ions. *J. Am. Chem. Soc.* **121**, 7360–7372.
- Bozin E. S., Schmidt M., DeConinck A. J., Paglia G., Mitchell J. F., Chatterji T., Radaelli P. G., Proffen T. and Billinge S. J. L. (2007) Understanding the insulating phase in colossal magnetoresistance manganites: shortening of the Jahn-Teller long-bond across the phase diagram of La_{1-x}Ca_xMnO₃. *Phys. Rev. Lett.* **98**, 137203.
- Brown I. D. (2009) Recent developments in the methods and applications of the bond valence model. *Chem. Rev.* **109**, 6858–6919.
- Brown I. D. and Altermatt D. (1985) Bond-valence parameters obtained from a systematic analysis of the Inorganic Crystal Structure Database. *Acta Crystallogr. B* **41**, 244–247.
- Chen R., Zavalij P. and Whittingham M. S. (1996) Hydrothermal synthesis and characterization of KMnO₄·yH₂O. *Chem. Mater.* **8**, 1275–1280.
- Chukhrov F. V., Gorshkov A. I., Beresovskaya V. V. and Sivtsov A. V. (1979) Contributions to the mineralogy of authigenic manganese phases from marine manganese deposits. *Miner. Deposita* **14**, 249–261.
- Chukhrov F. V., Gorshkov A. I., Rudnitskaya E. S., Beresovskaya V. V. and Sivtsov A. V. (1980) Manganese minerals in clays – a review. *Clay Clay Miner.* **28**, 346–354.
- Chupas P. J., Qiu X., Hanson J. C., Lee P. L., Grey C. P. and Billinge S. J. L. (2003) Rapid-acquisition pair distribution function (RA-PDF) analysis. *J. Appl. Crystallogr.* **36**, 1342–1347.
- Drits V. A., Silvester E., Gorshkov A. I. and Manceau A. (1997) Structure of synthetic monoclinic Na-rich birnessite and hexagonal birnessite: I. Results from X-ray diffraction and selected-area electron diffraction. *Am. Mineral.* **82**, 946–961.
- Drits V. A., Lanson B. and Gaillot A.-C. (2007) Birnessite polytype systematics and identification by powder X-ray diffraction. *Am. Mineral.* **92**, 771–788.

- Engami T. and Billinge S. J. L. (2003) *Underneath The Bragg Peaks Structural Analysis of Complex Materials*. Pergamon, Oxford, UK.
- Farrow C. L. and Billinge S. J. L. (2009) Relationship between the atomic pair distribution function and small angle scattering: implications for modeling of nanoparticles. *Acta Crystallogr. A* **65**, 232–239.
- Farrow C. L., Juhas P., Liu J. W., Bryndin D., Božin E. S., Bloch J., Proffen T. and Billinge S. J. L. (2007) PDFfit2 and PDFgui: computer programs for studying nanostructure in crystals. *J. Phys.: Condens. Mat.* **19**, 335219.
- Farrow C. L., Shaw M., Kim H., Juhas P. and Billinge S. J. L. (2011) Nyquist-Shannon sampling theorem applied to refinements of the atomic pair distribution function. *Phys. Rev. B* **84**, 134105.
- Favre-Nicolin V. and Cerny R. (2002) FOX, 'free objects for crystallography': a modular approach to *ab initio* structure determination from powder diffraction. *J. Appl. Cryst.* **35**, 734–743.
- Feng Q., Kanoh H., Miyai Y. and Ooi K. (1995) Alkali metal ions insertion/extraction reactions with hollandite-type manganese oxide in the aqueous phase. *Chem. Mater.* **7**, 148–153.
- Feng X., Zhai L., Tan W., Liu F. and He J. (2007) Adsorption and redox reactions of heavy metals on synthesized Mn oxide minerals. *Environ. Pollut.* **147**, 366–373.
- Feng X. H., Zhu M., Ginder-Vogel M., Ni C., Parikh S. J. and Sparks D. L. (2010) Formation of nano-crystalline todorokite from biogenic Mn oxides. *Geochim. Cosmochim. Acta* **74**, 3232–3245.
- Gaillot A.-C., Drits V. A., Manceau A. and Lanson B. (2007) Structure of the synthetic K-rich phylломanganate birnessite obtained by high-temperature decomposition of KMnO₄ substructures of K-rich birnessite from 1000 °C experiment. *Microporous Mesoporous Mater.* **98**, 267–282.
- Gateshki M., Hwang S.-J., Park D. H., Ren Y. and Petkov V. (2004) Structure of nanocrystalline alkali metal manganese oxides by the atomic pair distribution function technique. *J. Phys. Chem. B* **108**, 14956–14963.
- Gilbert B. (2008) Finite size effects on the real-space pair distribution function of nanoparticles. *J. Appl. Crystallogr.* **41**, 554–562.
- Giovanoli R. (1980) Vernadite is random-stacked birnessite. *Miner. Deposita* **15**, 251–253.
- Grangeon S., Lanson B., Lanson M. and Manceau A. (2009) Crystal structure of Ni-sorbed synthetic vernadite: a powder X-ray diffraction study. *Mineral. Mag.* **72**, 1279–1291.
- Grangeon S., Lanson B., Miyata N., Tani Y. and Manceau A. (2010) Structure of nanocrystalline phylломanganates produced by freshwater fungi. *Am. Mineral.* **95**, 1608–1616.
- Guinier A. (1963) *X-ray Diffraction in Crystals, Imperfect Crystals, and Amorphous Bodies*. W.H. Freeman, San Francisco.
- Guinier A., Fournet G., Walker C. and Yudowitch K. (1955) *Small-angle scattering of X-rays*. John Wiley & Sons, Inc., New York.
- Hammersley A. P., (1998) ESRF Internal Report, **ESRF98HA01T**, FIT2D V9.129 Reference Manual V3.1.
- Hochella M., Moore J. N., Putnis C. V., Putnis A., Kasama T. and Eberl D. D. (2005) Direct observation of heavy metal-mineral association from the Clark Fork River Superfund Complex: implications for metal transport and bioavailability. *Geochim. Cosmochim. Acta* **69**, 1651–1663.
- Kim H. S., Pasten P. A., Gaillard J. F. and Stair P. C. (2003) Nanocrystalline todorokite-like manganese oxide produced by bacterial catalysis. *J. Am. Chem. Soc.* **125**, 14284–14285.
- Lafferty B. J., Ginder-Vogel M., Zhu M., Livi K. J. T. and Sparks D. L. (2010) Arsenite oxidation by a poorly-crystalline manganese-oxide. 2. Results from X-ray absorption spectroscopy and X-ray diffraction. *Environ. Sci. Technol.* **44**, 8467–8472.
- Lanson B., Drits V. A., Silvester E. and Manceau A. (2000) Structure of H-exchanged hexagonal birnessite and its mechanism of formation from Na-rich monoclinic buserite at low pH. *Am. Mineral.* **85**, 826–838.
- Lanson B., Drits V. A., Feng Q. and Manceau A. (2002) Structure of synthetic Na-birnessite: evidence for a triclinic one-layer unit cell. *Am. Mineral.* **87**, 1662–1671.
- Lei M., de Graff A. M. R., Thorpe M. F., Wells S. A. and Sartbaeva A. (2009) Uncovering the intrinsic geometry from the atomic pair distribution function of nanomaterials. *Phys. Rev. B* **80**, 024118.
- Luther G. (2002) Kinetics of the abiotic reduction of polymeric manganese dioxide by nitrite: an anaerobic nitrification reaction. *Aquat. Geochem.* **8**, 15–36.
- Manceau A., Gorshkov A. I. and Drits V. A. (1992a) Structural chemistry of Mn, Fe, Co, and Ni in manganese hydrous oxides: Part I. Information from XANES spectroscopy. *Am. Mineral.* **77**, 1133–1143.
- Manceau A., Gorshkov A. I. and Drits V. A. (1992b) Structural chemistry of Mn, Fe, Co, and Ni in manganese hydrous oxides: Part II. Information from EXAFS spectroscopy and electron and X-ray diffraction. *Am. Mineral.* **77**, 1144–1157.
- Masadeh A. S., Božin E. S., Farrow C. L., Paglia G., Juhas P., Billinge S. J. L., Karkamkar A. and Kanatzidis M. G. (2007) Quantitative size-dependent structure and strain determination of CdSe nanoparticles using atomic pair distribution function analysis. *Phys. Rev. B* **76**, 115413.
- McKenzie R. M. (1971) The synthesis of birnessite, cryptomelane, and some other oxides and hydroxides of manganese. *Mineral. Mag.* **38**, 493–502.
- McKenzie R. M. (1980) The adsorption of lead and other heavy metals on oxides of manganese and iron. *Aust. J. Soil Res.* **18**, 61–73.
- Murray J. W. (1975) The interaction of metal ions at the manganese dioxide-solution interface. *Geochim. Cosmochim. Acta* **39**, 505–519.
- Perez-Benito J. F., Brillas E. and Pouplana R. (1989) Identification of a soluble form of colloidal manganese(IV). *Inorg. Chem.* **28**, 390–392.
- Petkov V., Trikalitis P. N., Bozin E. S., Billinge S. J. L., Vogt T. and Kanatzidis M. G. (2002) Structure of V₂O₅·nH₂O xerogel solved by the atomic pair distribution function technique. *J. Am. Chem. Soc.* **124**, 10157–10162.
- Petkov V., Ren Y., Saratovsky I., Pastern P., Gurr S. J., Hayward M. A., Poeppelmeier K. R. and Gaillard J. F. (2009) Atomic-scale structure of biogenic materials by total X-ray diffraction: a study of bacterial and fungal MnO_x. *ACS Nano* **3**, 441–445.
- Post J. E. (1999) Manganese oxide minerals: crystal structures and economic and environmental significance. *Proc. Nat. Acad. Sci. U.S.A.* **96**, 3447–3454.
- Post J. E., Heaney P. J. and Ertl A. (2008) Rietveld refinement of the ranciéite structure using synchrotron powder diffraction data. *Powder Diffr* **23**, 10–14.
- Qiu X., Thompson J. W. and Billinge S. J. L. (2004) PDFgetX2: a GUI-driven program to obtain the pair distribution function from X-ray powder diffraction data. *J. Appl. Crystallogr.* **37**, 1.
- Qiu X., Proffen T., Mitchell J. F. and Billinge S. J. L. (2005) Orbital correlations in the pseudocubic O and rhombohedral R phases of LaMnO₃. *Phys. Rev. Lett.* **94**, 177203.
- Ramstedt M., Andersson B. M., Shchukarev A. and Sjöberg S. (2004) Surface properties of hydrous manganite (r-MnOOH). A potentiometric, electroacoustic, and X-ray photoelectron spectroscopy study. *Langmuir* **20**, 8224–8229.

- Rustad J. R., Felmy A. R., Rosso K. M. and Bylaska E. J. (2003) *Ab initio* investigation of the structures of NaOH hydrates and their Na⁺ and OH⁻ coordination polyhedra. *Am. Mineral.* **88**, 436–449.
- Saratovsky I., Wightman P. G., Pasten P. A., Gaillard J. F. and Poeppelmeier K. R. (2006) Manganese oxides: parallels between abiotic and biotic structures. *J. Am. Chem. Soc.* **128**, 11188–11898.
- Saratovsky I., Gurr S. J. and Hayward M. A. (2009) The Structure of manganese oxide formed by the fungus *Acremonium* sp. strain KR21–2. *Geochim. Cosmochim. Acta* **73**, 3291–3300.
- Shindo H. and Huang P. (1982) Roles of Mn(IV) oxide in abiotic formation of humic substances in the environment. *Nature* **298**, 363–365.
- Shindo H. and Huang P. (1984) Significance of Mn(IV) oxide in abiotic formation of organic nitrogen complexes in natural environments. *Nature* **308**, 57–58.
- Silvester E., Manceau A. and Drits V. A. (1997) Structure of synthetic monoclinic Na-rich birnessite and hexagonal birnessite: II. Results from chemical studies and EXAFS spectroscopy. *Am. Mineral.* **82**, 962–978.
- Stone A. T. and Morgan J. J. (1984) Reduction and dissolution of manganese(III) and manganese(IV) oxides by organics. 1. Reaction with hydroquinone. *Environ. Sci. Technol.* **18**, 450–456.
- Toby B. H. and Egami T. (1992) Accuracy of pair distribution function analysis applied to crystalline and non-crystalline materials. *Acta Crystallogr. A* **48**, 336–346.
- Villalobos M., Toner B., Bargar J. and Sposito G. (2003) Characterization of the manganese oxide produced by *Pseudomonas putida* strain MnB1. *Geochim. Cosmochim. Acta* **67**, 2649–2662.
- Villalobos M., Lanson B., Manceau A., Toner B. and Sposito G. (2006) Structural model for the biogenic Mn oxide produced by *Pseudomonas putida*. *Am. Mineral.* **91**, 489–502.
- Webb S. M., Tebo B. M. and Bargar J. R. (2005a) Structural characterization of biogenic Mn oxides produced in seawater by the marine *Bacillus* sp. strain SG-1. *Am. Mineral.* **90**, 1342–1357.
- Webb S. M., Tebo B. M. and Bargar J. R. (2005b) Structural influences of sodium and calcium ions on the biogenic manganese oxides produced by the marine *Bacillus* sp. strain SG-1. *Geomicrobiol. J.* **22**, 181–193.
- Wehrli B., Friedl G. and Manceau A. (1995) Reaction rates and products of manganese oxidation at the sediment-water interface. In *Aquatic Chemistry: Interfacial and Interspecies Processes* (eds. Chin Pao Huang, Charles R. O'Melia and James Morgan), vol. 224, American Chemical Society, Washington, DC, pp. 111–134.
- Yang D. S. and Wang M. K. (2001) Syntheses and characterization of well-crystallized birnessite. *Chem. Mater.* **13**, 2589–2594.
- Yang D. S. and Wang M. K. (2002) Syntheses and characterization of birnessite by oxidizing pyrochroite in alkaline conditions. *Clays Clay Miner.* **50**, 63–69.
- Zhang H., Chen B. and Banfield J. F. (2009) The size dependence of the surface free energy of titania nanocrystals. *Phys. Chem. Chem. Phys.* **11**, 2553–2558.
- Zhu M., Paul K. W., Kubicki J. D. and Sparks D. L. (2009) Quantum chemical study of arsenic (III, V) adsorption on Mn-oxides: implications for arsenic(III) oxidation. *Environ. Sci. Technol.* **43**, 6655–6661.
- Zhu M., Ginder-Vogel M., Parikh S. J., Feng X.-H. and Sparks D. L. (2010a) Cation effects on the layer structure of biogenic Mn-oxides. *Environ. Sci. Technol.* **44**, 4465–4471.
- Zhu M., Ginder-Vogel M. and Sparks D. L. (2010b) Ni(II) sorption on biogenic Mn-oxides with varying Mn octahedral layer structure. *Environ. Sci. Technol.* **44**, 4472–4478.

Associate editor: Kevin M. Rosso